Influence of Electrowetting on Glycine Polymorphic Form in Evaporative Crystallization of Sessile Droplets

An, Q.; Cui, P.; Nagalingam, Nagaraj; Binan, N.K.; Bera, B.; Mastrangeli, Massimo; Padding, J.T.; Eral, H.B.

DOI
10.1021/acs.cgd.5c00497

Publication date
2025

Document Version
Final published version

Published in
Crystal Growth & Design

Citation (APA)
An, Q., Cui, P., Nagalingam, N., Binan, N. K., Bera, B., Mastrangeli, M., Padding, J. T., & Eral, H. B. (2025). Influence of Electrowetting on Glycine Polymorphic Form in Evaporative Crystallization of Sessile Droplets. *Crystal Growth & Design*, *25*(17), 7123-7132. https://doi.org/10.1021/acs.cgd.5c00497

CRYSTAL GROWTH & DESIGN

pubs.acs.org/crystal

Article

Influence of Electrowetting on Glycine Polymorphic Form in Evaporative Crystallization of Sessile Droplets

Qi An, Pingping Cui, Nagaraj Nagalingam, Noah Binan, Bijoy Bera, Massimo Mastrangeli, Johan T. Padding, and Hüseyin Burak Eral*

Cite This: *Cryst. Growth Des.* 2025, 25, 7123−7132

Read Online

ACCESS | Metrics & More | Article Recommendations | Supporting Information

ABSTRACT: We investigated the evaporative crystallization of aqueous glycine sessile droplets on hydrophilic glass, hydrophobic Teflon surfaces, and hydrophobic Teflon surfaces, where the contact angle is manipulated dynamically with electrowetting. Microscopy experiments and analytical characterization revealed that the size, morphology, and polymorphic form (α, β, and γ) of the glycine crystals are influenced by the surface wettability as well as the amplitude and frequency of electrowetting. On a hydrophilic glass surface, a coffee-stain-shaped residue composed of a mixture of bipyramidal α and needle-like β crystals was observed. On a hydrophobic Teflon surface, the droplets evaporated with minimum contact line pinning, producing hemispherical residue shapes, and bipyramidal α crystals smaller than 100 μm were formed. On a Teflon surface with electrowetting, glycine could be manipulated to crystallize into distinct polymorphic forms (β and γ) and residue shapes not observed on hydrophilic glass and hydrophobic Teflon surfaces. The frequency and amplitude of electrowetting were optimized to produce single large crystals. We observed the highest chance of producing single-millimeter-scale crystals at a frequency of 1 kHz and a voltage amplitude of 80 V_{rms}. We attribute this observation to a combination of nucleation at lower bulk supersaturation compared to the experiment on Teflon surfaces and electrowetting-induced mixing most prominent at 1 kHz. Our results highlight the opportunities arising from the dynamic manipulation of surface wettability.

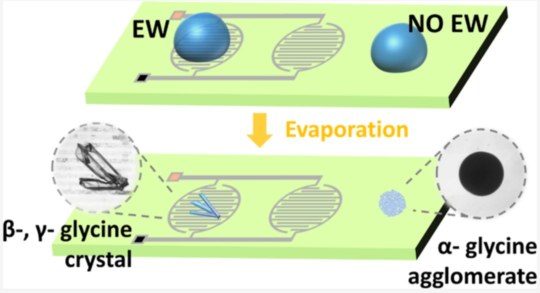

INTRODUCTION

Polymorphism is the phenomenon in which molecules can crystallize into distinct molecular unit cells. It significantly influences the relevant physical properties in pharmaceuticals such as solubility and bioavailability. This variability often leads to differences in solubility of the drug in the body, altering the efficacy of the drug and causing major challenges in drug development. Therefore, the control of polymorphism is of great importance. Traditional polymorph screening methods include cooling, evaporative, antisolvent, and reactive crystallization.[1,2] More recently, advanced techniques based on electric fields,[3−5] ultrasound,[6−8] acoustic waves,[9] templates,[10,11] and laser-induced nucleation[12−14] have been developed. When conducting polymorph screening experiments, various parameters, such as combinations of different solvents and concentrations of active pharmaceutical ingredients (APIs), can be adjusted.[15] Thus, high-throughput screening (HTS) becomes important since it provides a systematic approach to effectively explore the polymorphic landscape of APIs.[16−18]

One common approach in high-throughput screening involves depositing minute-volume solutions containing the API and solvent onto surfaces. The deposited sessile droplets evaporate, and the resulting crystals are characterized to identify the polymorphic form emerging from the solution. This process may be crucial for rapidly and comprehensively identifying all accessible polymorphic forms of a compound under various crystallization conditions. Identifying all of the accessible forms enables the selection of a stable and pharmaceutically suitable crystal form, improving the consistency of the product. However, the influence of surface wettability on this process is often overlooked. Surface wettability and the evaporation process collectively affect the patterns of the deposited residues. Therefore, a deeper understanding of evaporation-induced patterns is beneficial for HTS techniques, particularly those utilizing liquid-handling robotics or inkjet printing to deposit sessile droplets on surfaces.

Glycine, the simplest amino acid, is widely used as a model compound due to its multiple polymorphic forms. Under atmospheric temperature and pressure, it has three polymorphs, referred to as α, β, and γ. α- and γ-glycine remain stable, whereas metastable β-glycine crystals gradually trans-

Received: April 7, 2025
Revised: August 5, 2025
Accepted: August 6, 2025
Published: August 19, 2025

https://doi.org/10.1021/acs.cgd.5c00497
Cryst. Growth Des. 2025, 25, 7123−7132

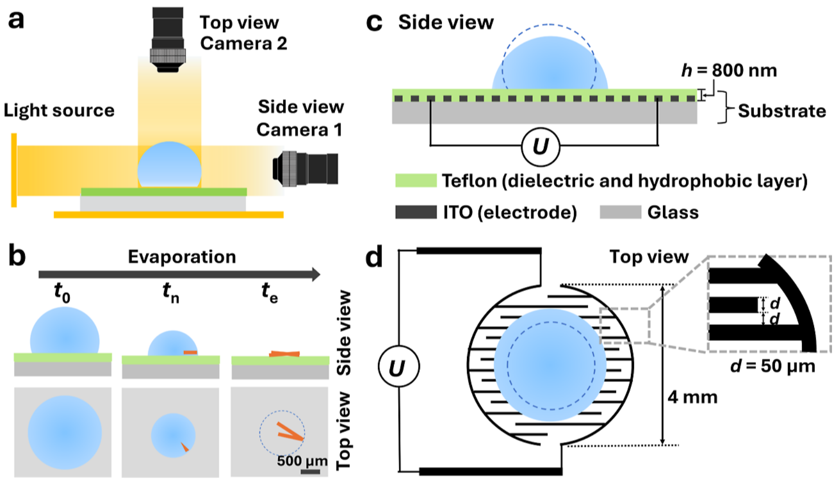

Figure 1. Schematic of the experimental setup. (a) Droplet evaporation is monitored using two cameras, capturing both side and top views. Sessile droplets (5.0 μL) of aqueous glycine solution (0.5 M), with a base diameter of approximately 2 mm, were used in all experiments. (b) Illustration of the sessile droplet evaporation from side and top views. At t_0, the droplet is placed on the substrate. As the droplet evaporates, the concentration of the solute increases. The first crystal is observed at t_n, and complete crystallization occurs at t_e. (c) The side view of a droplet on Teflon-coated ITO glass (**Teflon-EW**) illustrates the droplet without an applied voltage (dashed line) and with an applied voltage. (d) Top view of the droplet on the substrate, showing interdigitated electrodes with a width and gap of d (d = 50 μm). The thickness of the Teflon dielectric layer is denoted as h, h = 800 nm. Illustration not to scale.

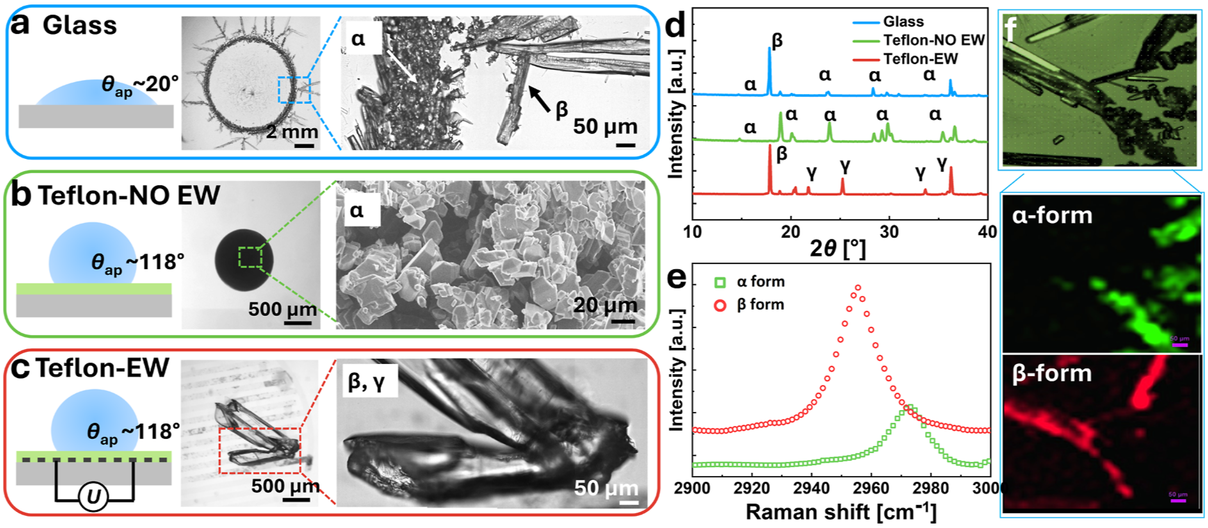

Figure 2. Residue shape on **Glass**, **Teflon-NO EW**, and **Teflon-EW**, with polymorphism characterization of glycine crystals. (a−c) Side-view schematics show three cases of 5.0 μL sessile droplets of glycine solution (0.5 M) at the initial stage, with top-view optical images of the formed crystal residues after evaporation. (a) Evaporation on a hydrophilic glass slide with an initial contact angle of 20° (**Glass**). (b) Evaporation on hydrophobic Teflon-coated ITO glass with an initial contact angle of 118° (**Teflon-NO EW**). (c) Evaporation on Teflon-coated ITO glass with electrowetting by applying an electrical signal of 1 kHz, 60 V_{rms} (**Teflon-EW**). Before the voltage is turned on, the contact angle of the droplet on Teflon-coated ITO glass is 118°, as illustrated in panel (c). The contact angle decreases to 112° at 60 V_{rms}. The zoomed-in images in panels (a) and (c) are captured using an optical microscope, while the zoomed-in image in panel (b) is obtained from a scanning electron microscope. (d) PXRD characterization of glycine crystals obtained from three cases. (e) Raman spectra collected at two points on the final residue crystal in (a): one on the ring and another on the needle-like crystal, showing distinct α form and β form, identified by Raman peaks at 2973 cm^{-1} and 2952 cm^{-1}, respectively. (f) Raman mapping further illustrates the distribution of α-form (green) and long needle-like β-form (red) crystals after droplet evaporation on **Glass**.

form into α and/or γ forms.[19,20] Notably, β- and γ-glycine exhibit unique piezoelectric responses due to their non-centrosymmetric space groups.[21] Various studies showed control of the polymorphic form of glycine through evaporative crystallization of sessile droplets. For instance, it has been observed that evaporating microdroplets of glycine aqueous solution on different substrates leads to β-glycine crystals nucleated at the three-phase contact line, and the α form appears predominantly within the bulk of the droplet.[22,23] More recently, graphene has been used as a template to enhance glycine polymorph selectivity and screening, taking advantage of its tunable surface chemistry.[24] Additionally, He et al.[25] reported the formation of γ-glycine from an aqueous solution through slow evaporation. By further confining the crystallization space, patterned self-assembled monolayer (SAM) substrates have been introduced, which consist of hydrophilic islands surrounded by a hydrophobic region. On these micropatterned SAM substrates, all three polymorphic

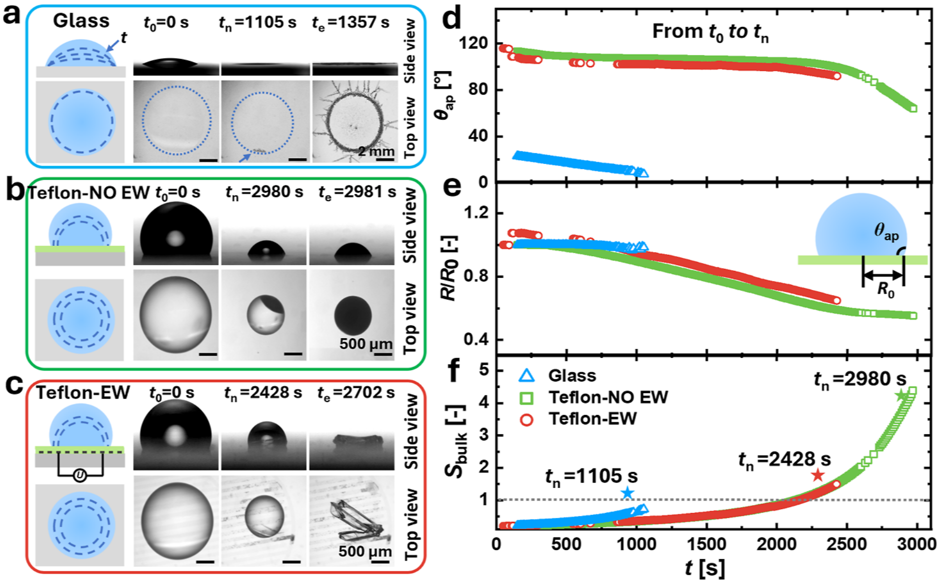

Figure 3. Time-lapse images of the evaporation and crystallization processes of 5.0 μL and 0.5 M glycine droplets from side and top views on (a) **Glass**, (b) **Teflon-NO EW**, and (c) **Teflon-EW**. Apparent contact angle (d), normalized contact radius (e), and average supersaturation (f) of bulk droplets as a function of time for various wetting regimes.

forms of glycine crystals were obtained, and the probability of each form can be adjusted by controlling the island size,[20] the evaporation rate,[26] or the pH of the solution.[27] Furthermore, advances in inkjet printing technology have made it possible to crystallize materials in confined picolitre volumes. Using this technique, isolated β-glycine crystals have been produced by depositing glycine picolitre droplets onto substrates via inkjet printing.[28,29] Despite these studies achieving isolated β-glycine, the methods require either complicated surface modification, space confinement, or additional solvent, which hinders their industrial implementation. Therefore, developing a simple, flexible, and tunable method for polymorph selection remains a significant challenge.

Electrowetting (EW) is a powerful tool for tuning surface wettability by applying an electric field. The classic Young–Lippmann equation can be used to describe the voltage-dependent contact angle (θ_{ap}) as[30]

$$\cos\theta_{ap} = \cos\theta_{eq} + \frac{\varepsilon_d\varepsilon_0}{2\gamma_{lg}h}U^2 \tag{1}$$

where θ_{ap} denotes the apparent contact angle in the absence of voltage; θ_{eq} denotes the equilibrium contact angle; ε_d, ε_0, and h are the relative permittivity, vacuum permittivity, and thickness of the dielectric layer; and γ_{lg} and U are the liquid–gas surface tension and the applied voltage, respectively. The electric field generates localized, well-controlled forces at the contact line, effectively overcoming the pinning forces of the droplet. Previous studies have shown that electrowetting can alter the deposition pattern of colloidal droplets by suppressing contact line pinning during the evaporation process.[31,32] This can be further applied in matrix-assisted laser desorption/ionization (MALDI) mass spectrometry to enhance the intensity of the MALDI signal, where small pharmaceutical molecules have been studied. However, the effects of electrowetting on the polymorphism of the final crystal residue have not been investigated.[33,34]

Here, we present the first report on controlling the size, morphology, and polymorphic form of glycine crystals nucleating from evaporating sessile droplets using electrowetting, as illustrated in Figure 1. Our study focuses on the role of dynamic surface wettability in the evaporation of sessile droplets in a model compound, glycine. On a hydrophilic glass surface (**Glass**), coffee-stain-shaped residues containing a mixture of α- and β-form crystals were observed (Figure 2a). On a hydrophobic Teflon surface, without electrowetting (**Teflon-NO EW**), the final residues primarily consisted of dense semispherical crystal agglomerates with an α-form crystalline structure (Figure 2b). In contrast, in the presence of electrowetting (**Teflon-EW**), the residues predominantly formed large single crystals with a γ-form crystalline structure (Figure 2c). The supersaturation, apparent contact angle, and contact radius of the droplet were analyzed by using time-lapse images of the evaporation process (Figure 3d–f). Additionally, the effects of voltage frequency and amplitude were systematically investigated.

■ EXPERIMENTAL SECTION

Materials. Glycine (99%, CAS 56-40-6, Sigma-Aldrich, NL), used as received without any further processing, exhibits an α form. Aqueous glycine solution (0.5 M) was prepared by dissolving 1.125 g of glycine in 30.0 g of deionized (DI) water obtained from the Milli-Q ultrapure water system (Merck). Isopropyl alcohol (IPA) and acetone, purchased from VWR Chemicals, were used for glass cleaning, and Teflon (AF 1601 X, Chemours, USA) was used for ITO glass coating.

Evaporation Experiments. A droplet of aqueous glycine solution was deposited on the substrate to evaporate spontaneously. The evaporation and crystallization process was monitored from both side and top views; the experimental setup is depicted in Figure 1a. All droplets in the experiments were 5.0 μL of a glycine solution (0.5 M). The initial solution was undersaturated. As the solvent evaporated, the concentration of glycine increased, leading to the formation of crystals (Figure 1b). The side and top views of the droplet on the substrate are shown in Figures 1c and 1d. The substrate consisted of Teflon-coated patterned indium tin oxide (ITO) glass, which functions as a dielectric and hydrophobic layer (Figure 1c). A wire-free electrowetting configuration was used to eliminate experimental issues arising from wire electrodes.[31] The ITO glass consists of a pattern with an electrode width and a gap of d (d = 50 μm, Figure 1d),

https://doi.org/10.1021/acs.cgd.5c00497
Cryst. Growth Des. 2025, 25, 7123–7132

fabricated using lithography. The effects of the electrode width and gap are not investigated in this work. However, due to the availability of substrate, electrodes with d = 100 μm were used in the experiment to study the effect of voltage amplitude on crystal polymorphism, as shown in Figure 4b.

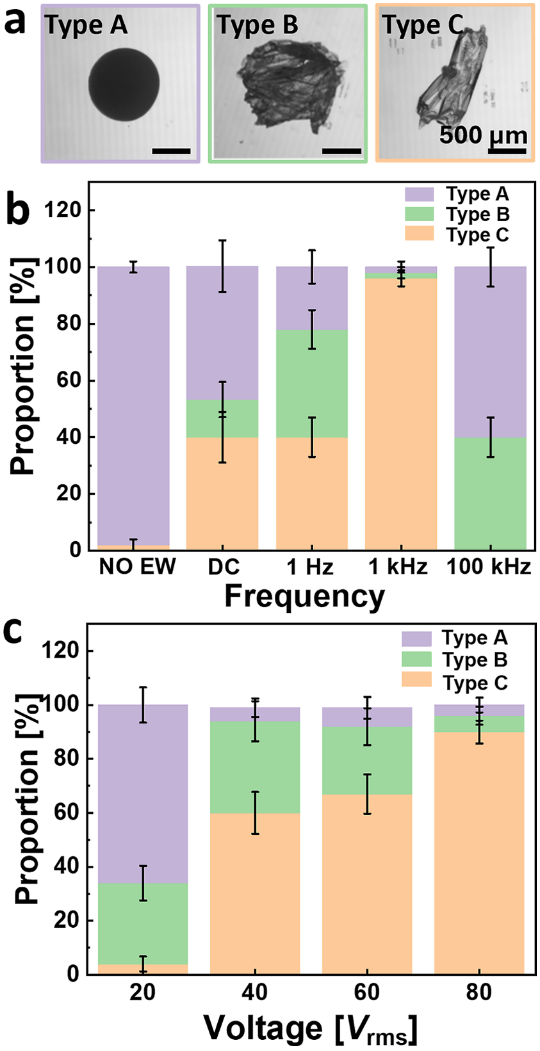

Figure 4. Residue types and their proportions on **Teflon-NO EW** and **Teflon-EW** under varying frequencies and voltage amplitudes. (a) Optical images of representative residues after evaporation, showing three types: Type A, Type B, and Type C, categorized by their shape and growth dynamics after the formation of the first nuclei. (b) The proportion of Type A, Type B, and Type C residues at different frequencies, with a fixed voltage amplitude of 60 V_{rms}. (c) The proportion of Type A, Type B, and Type C residues at different voltage amplitudes, with a fixed frequency of 1 kHz. Error bars are calculated using the standard error formula: $\mathrm{SE} = \sqrt{p_i(1 - p_i)/n}$, where p_i is the observed proportion for category i and n is the number of independent trials. Each frequency or amplitude condition was tested with 30–50 droplets (n = 30–50).

The substrate was prepared as follows: first, the patterned ITO glass was sequentially cleaned in an ultrasonic bath with acetone, IPA, and DI water for 20 min, followed by drying with nitrogen; subsequently, an 800 nm-thick layer of Teflon AF was spin-coated onto the ITO glass substrate using a spin coater (SPIN 150i, POLOS). The Teflon AF solution consisted of the amorphous fluoropolymer Teflon AF dissolved in Fluorinert FC-40. After spin coating, the substrate was heated on a hot plate at 160 °C for 10 min to remove the solvent and form a hydrophobic Teflon AF coating. For simplicity, this coating is termed the Teflon layer throughout the text. A Teflon layer is commonly used in electrowetting applications as it prevents electrolysis and ensures a high initial contact angle.[35] The average initial contact angle of the droplet on the Teflon surface was measured to be 118° using the Optical Contact Angle Measurement System (OCA 25, Dataphysics Instruments).

The droplets were subjected to electrowetting throughout the entire evaporation process. An alternating voltage (20–80 V_{rms}) with frequencies ranging from 1 Hz to 100 kHz was applied by a function generator (RSDG800, RS PRO) and amplified through a WMA-100A high-voltage amplifier (Falco Systems). We refer to the case of droplets evaporating on the hydrophobic Teflon-coated surface under electrowetting as **Teflon-EW**. Additionally, droplets on the same Teflon-coated surface without electrowetting are referred to as **Teflon-NO EW**. The droplet evaporation on a hydrophilic glass surface, with an average initial contact angle of 20°, is referred to as **Glass**. The glass substrate was prepared by cleaning microscope glass slides (Fischer Scientific) in an ultrasonic bath using the same protocol as for the ITO glass.

Experiments were conducted under controlled conditions with an ambient temperature of 20 ± 1 °C and a relative humidity level of 35 ± 5%. The substrate was covered with a box (10 × 10 × 6 cm; $L \times W \times H$) to block air currents. The apparent contact angle (θ_{ap}), the contact radius (R), and the volume (V) of the droplet were recorded and analyzed from camera 1 (side view) from the OCA system. The volume of the droplet was automatically collected using the instrument's SCA software. The software assumes the droplet to be a spherical cap and calculates its volume by integrating the area under the fitted curve. To validate this method, we compared the volume calculated by software (4.8 μL) with the volume dispensed by a pipet (5.0 μL), resulting in a 4% error. The crystallization process was captured using a camera 2 (U3-3880SE-M-GL, IDS Imaging) from the top view.

Morphology and Polymorphism Characterization. The morphology of the formed crystals was characterized by using an optical microscope (Eclipse Ti2-E, Nikon) and a field emission scanning electron microscope (JSM-6500F, JEOL Ltd.). Crystals were transferred with tweezers onto adhesive carbon tape affixed to a SEM sample holder without sputter coating. SEM images were acquired at an accelerating voltage of 10.0 kV and a magnification of 500×.

Raman microscopy (LabRAM Evolution HR, Horiba) and powder X-ray diffraction (PXRD; D2 Phaser, Bruker) were used to identify the crystal polymorphs. Raman spectra were collected in the wavenumber range of 2900–3000 cm^{-1} using a 515 nm laser and a 50× objective lens, with an acquisition time of 10 s and 3 accumulations. The theoretical spot size ($0.61\lambda/\mathrm{NA}$) is approximately 500 nm (λ = 515 nm, NA = 0.6). For each sample, Raman measurements were repeated five times at different positions on the crystals. PXRD measurements were taken in the 2θ range of 10–40°, with an angular increment of 0.06° per second, at 30 kV and 10 mA. Since an individual crystal residue (~0.2 mg) was insufficient for PXRD analysis, 10 residues obtained under the same experimental conditions were collected together for PXRD analysis. The crystal residues were gently broken into smaller fragments using tweezers and evenly spread, concentrating the crystals in the center of the sample holder.

■ RESULTS AND DISCUSSION

Droplet Evaporation and Crystallization. The crystal residues formed after droplet evaporation under the three different conditions—**Glass**, **Teflon-NO EW**, and Teflon EW—are shown in Figures 2a–c, respectively. On a glass surface, droplets of glycine solution exhibited low contact angles of around 20° (Figure 2a, **Glass**). After spontaneous evaporation in the ambient environment, the crystals formed a coffee-stain pattern with bipyramidal α-form crystals along the contact line, while the outward branches consisted of β-form dendritic crystals. The polymorphism was characterized by PXRD (Figure 2d, blue pattern) and Raman microscopy (Figure 2e,f). These results are consistent with observations reported in other studies,[23,28] where glycine droplets evaporated on glass surfaces and α- and β-form glycine crystals were observed to nucleate at the contact line. Notably, Buanz and Gaisford[28] also reported the formation of a coffee-stain-shaped crystal residue of glycine on glass. The coffee-stain shape refers to a ring-like deposition pattern that remains after a droplet containing suspended particles (e.g., a droplet of coffee) dries on a solid surface.[36] On a Teflon surface, the droplet of glycine solution exhibited an initial contact angle of 118° (Figure 2b, **Teflon-NO EW**). The resulting crystals formed a hemispherical agglomerate, which appeared as a black circular pattern from the top view. SEM revealed that the agglomerate consisted of tiny crystals ranging in size from several to tens of micrometers. (zoomed-in image in panel (b)). PXRD analysis (Figure 2d, green pattern) confirmed that only the α form was present in the **Teflon-NO EW** cases. On a Teflon surface, with electrowetting (1 kHz, 40 V_{rms}) applied continuously throughout the entire evaporation and crystallization process, a residue consisting of single large millimeter-scale rod-shaped crystals was formed (Figure 2c, **Teflon-EW**). PXRD (Figure 2d, red pattern) revealed the presence of both the β and γ forms, marking a significant shift in crystal morphology and polymorphism compared with the previous two cases. Thus, we observed that electrowetting has a profound effect on both the morphology and polymorphism of the glycine crystals formed through the evaporative crystallization process.

The droplet evaporation and, consequently, the crystallization process were monitored both from the side and from the top view. Time-lapse images in Figure 3a−c present the process under three conditions: **Glass**, **Teflon-NO EW**, and **Teflon-EW**, respectively. We illustrate the process by highlighting three key time points: (i) the initial state (t_0), (ii) the time when crystals nucleated and grew to an observable size (t_n), and (iii) the point at which crystallization is complete (t_e). From t_0 to t_n, the apparent contact angle (θ_{ap}), the normalized contact radius (R/R_0), and the average supersaturation (S_{bulk}) of the bulk droplets as a function of time for the three cases were analyzed (Figure 3d−f). The bulk supersaturation is given by

$$S_{\mathrm{bulk}} = \frac{C_{\mathrm{bulk}}}{C_{\mathrm{sat}}} \tag{2}$$

where C_{sat} is the saturated concentration of glycine (22.5 g/100 g water, 20 °C),[37] and the average bulk concentration C_{bulk} is derived from the droplet volume:

$$C_{\mathrm{bulk}} = \frac{V_0 C_0}{V_t} \tag{3}$$

with V_0 and C_0 being the initial volume and concentration of the droplet, respectively, and V_t the droplet volume at time t. The volume of the droplet was automatically collected by using SCA software. The software assumes the droplet to be a spherical cap and calculates its volume by integrating the area under the fitted curve.

In the case denoted as **Glass**, initially, the crystal nucleated at the three-phase contact line (blue arrow in Figure 3a) and then formed a ring-shaped residue along the contact line. Subsequently, dendritic crystals grew outward from the contact line, forming branches (see Video S1 in the Supporting Information). As shown in Figures 3d and 3e (blue triangles), the decrease in contact angle, while the normalized contact radius remained constant, confirms the presence of contact line pinning.[38] This pinning led to solvent migration toward the edge, transporting glycine molecules to the contact line, driven by capillary flow.[36,39] Consequently, a higher local concentration and supersaturation occurred at the contact line. Despite the average supersaturation of the droplet being below 1 at the onset of nucleation (blue star in Figure 3f), nucleation was observed because the local supersaturation at the contact line exceeded that of the bulk liquid. Notably, the contact radius of the droplet on glass was larger than the other two cases due to the lower contact angle. The initial contact radius of the droplets on the glass and Teflon surfaces was approximately 2.5 mm and 1.0 mm, respectively.

In the case denoted as **Teflon-NO EW**, the droplet nucleated at the three-phase contact line and solidified within 1 s, forming agglomerates (from t_n to t_e, Figure 3b). A similar phenomenon was also observed by Wu et al.[40] No contact line pinning is observed during the evaporation process. As demonstrated in Figures 3d and 3e (green squares), the normalized contact radius decreased, while the contact angle remained unchanged. Toward the end, the contact radius stabilized and the contact angle decreased, indicating an initial receding contact line followed by contact line pinning. This behavior can be attributed to the low contact angle hysteresis (<10°) on the Teflon surface.[30] As shown in Figure 3f, the bulk supersaturation at the onset of nucleation (green star) was approximately at S_{bulk} equal to 4.5 (t_n = 2980 s), which is significantly higher than in the case of **Glass** and **Teflon-EW**. This indicates that nucleation occurred later and at a higher average supersaturation, resulting in more nuclei, which in turn led to smaller crystal sizes and a faster crystal growth rate.[41,42]

In the case denoted as **Teflon-EW**, from Figures 3d and 3e (red circle), the behavior here closely parallels that of the **Teflon-NO EW** case. The contact angles of **Teflon-EW** were slightly lower than those of **Teflon-NO EW** due to the effect of electrowetting. This is reflected by a 6° jump of the contact angle in the early stage (also shown in Figure S1), resulting in a slightly larger normalized base diameter compared to **Teflon-NO EW**. However, this small difference in contact angle is insufficient to cause a significant change in evaporation rate, and hence, the slopes of S (Figure 3f) remain similar for both **Teflon-NO EW** and **Teflon-EW**. Compared to **Teflon-NO EW**, crystals nucleated and grew to an observable size at an earlier time. We can conclude that the nucleation and growth processes are collectively faster in the presence of electrowetting. However, it is not possible to conclude which one of these two fundamental phenomena dominates from this observation. Additionally, the supersaturation at t_n is lower (around 1.5), allowing for a longer crystal growth process and resulting in larger crystals compared to **Teflon-NO EW** (see Videos S2 and S3 in Supporting Information). The crystals grew laterally along the surface with no observed correlation between the crystal growth direction and the electrode pattern. From Figure 3, we can conclude that from the evaporation process (t_0 to t_n), **Teflon-NO EW** and **Teflon-EW** exhibited similar evaporation modes, while **Glass** shows a different evaporation mode due to contact line pinning.

Morphology and Polymorphism Control by EW. The effect of electrowetting on the final residue was investigated by controlling the frequency and amplitude of the applied voltage

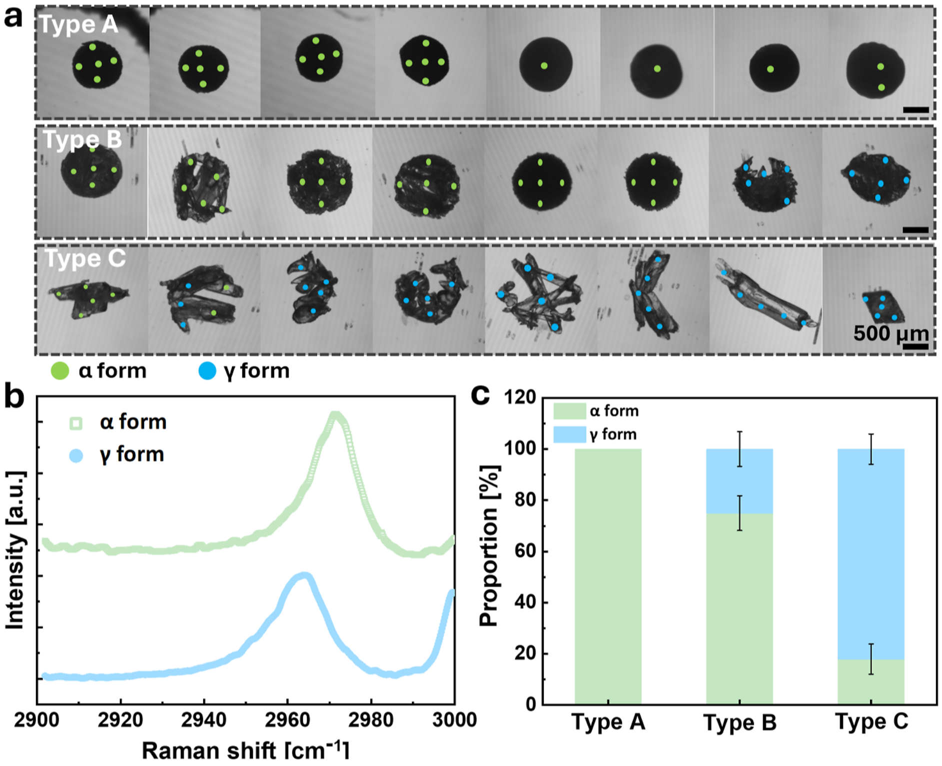

Figure 5. (a) Top view of the final residues selected from each type for Raman characterization after 16 days of storage, with dots indicating the Raman measurement sites. Green dots represent the *α* form, while blue dots indicate the *γ* form. (b) Representative Raman spectra of the final residue crystals. (c) Proportion of *α* form and *γ* form as a function of residue type.

on Teflon-coated surfaces (**Teflon-EW**). We varied the frequency from 1 Hz to 100 kHz at a fixed amplitude of 60 V_{rms}, and the amplitude from 20 to 80 V_{rms} at a fixed frequency of 1 kHz. For each experimental condition, 30−50 droplets were studied. Based on the formation and shape of the residue, we classified the residues into three groups, with representative images shown in Figure 4a, and more images are shown in Figures S3 and S4. The two extreme morphologies were opaque, hemispherical agglomerates (referred to as Type A) and transparent single crystals (referred to as Type C). Between these extremes, we identified residues with distinct characteristics, which we refer to as Type B. Time-lapse images of the droplet crystallization process provide further insight into these three types (Figure S2). For Type A, within 1 s (from t_{n} to t_{e}), the entire droplet transforms into an opaque solid, consisting of many small crystals on the order of tens of micrometers. In contrast, Type B residues contain larger crystals and complete crystallization in about 100 s, forming translucent crystal agglomerates. Type C, on the other hand, consists of one or a few nuclei that grow slowly, with the crystallization process taking much longer—more than 800 s.

Figure 4b,c presents the percentages of each type of residue as a function of different frequencies and amplitudes. Each frequency or amplitude condition in Figure 4b,c was tested with 30−50 droplets; the images of all final residues are provided in Figures S3 and S4. From Figure 4b, without electrowetting (**Teflon-NO EW**), the residues are predominantly Type A. The probability of forming a Type A crystal residue is estimated to be between 94.1% and 100.0% with a 95% confidence level. By contrast, with electrowetting at 1 kHz, most residues are Type C, with a significantly higher proportion than in the other cases. The probability of forming a Type C crystal residue under 1 kHz is estimated to be between 90.6% and 100.0% with a 95% confidence level. Therefore, we consider 1 kHz to be the optimized frequency and then fix it while varying the amplitude. In Figure 4c, increasing the amplitudes leads to a higher percentage of Type C residues, while the percentage of Type A residues decreases. This demonstrates a clear voltage dependence of the residue type, indicating that both the frequency and the amplitude of the applied voltage play crucial roles in the final shape of glycine crystal residues.

To further analyze the polymorphism of the final residues, we randomly collected 8 residues from each residue type provided in Figure 4a and selected five random points (green and blue dots) on each residue for Raman characterization, as shown in Figure 5a. A representative spectrum is presented in Figure 5b, where Raman peaks at 2973 cm^{-1} and 2963 cm^{-1} correspond to the *α* and *γ* forms, respectively. To visualize the polymorphic form within each type, the Raman measurement sites are marked in Figure 5a, with green dots representing *α*-form glycine crystals and blue dots indicating the *γ* form. Figure 5c shows the proportion of *α* form and *γ* forms in each residue type identified by Raman microscopy, revealing that Type A residues consist entirely of *α*-form glycine. This result is consistent with the PXRD analysis (green pattern in Figure 2d), in which 10 Type A crystal residues were collected for a single PXRD measurement. Both PXRD and Raman analyses show the *α* form. Overall, identification of the polymorphic form of single residues by Raman agrees with the collective polymorphic identification of 10 residues by PXRD. It should be noted that the mass of a single crystal residue was insufficient for PXRD analysis; thus, only Raman microscopy

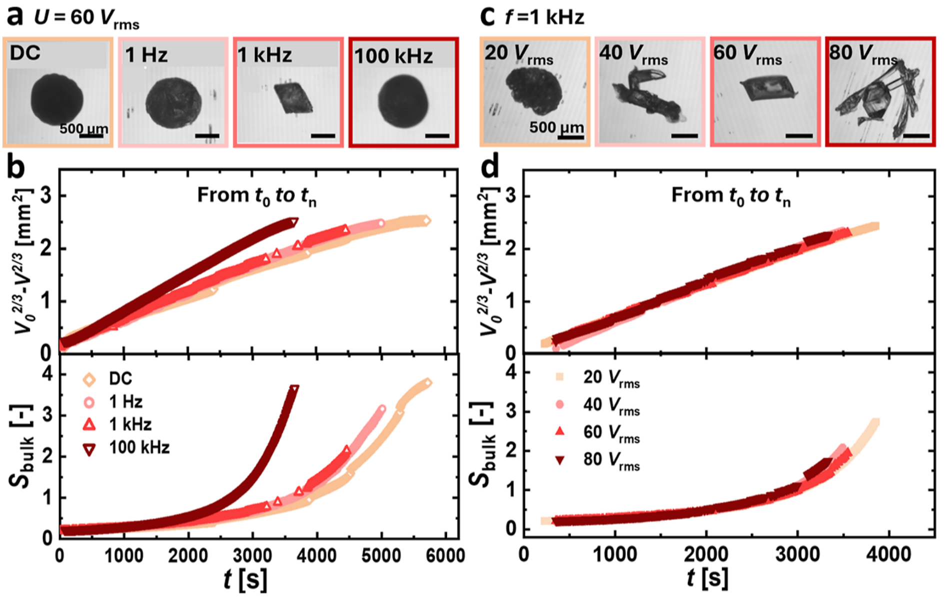

Figure 6. Experiments conducted at various frequencies and voltage amplitudes. (a) Top-view images of the final residues from experiments with a fixed voltage amplitude of 60 V_{rms} and varying frequencies. (b) Corresponding volume loss and supersaturation of bulk droplets over time, from the initial stage to nucleation. (c) Top-view images of the final residues from experiments with a fixed frequency of 1 kHz and varying voltage amplitudes. (d) Corresponding volume loss and average supersaturation of bulk droplets as functions of time.

provides polymorphic information at the single-residue level. In contrast, Type C residues are predominantly of the γ form.

In summary, at 1 kHz and 80 V_{rms}, the residues are predominantly Type C, primarily consisting of the γ form. In contrast, without electrowetting (as shown in Figure 3b), most residues are Type A, corresponding to the α form. Notably, Raman characterization was performed after 16 days of storage (stored in a sealed box at room temperature and ambient humidity). In the fresh sample, some points initially exhibited the β form. However, upon reexamining the same points after 16 days, all β forms had transformed into either α or γ form, as shown in Figure S6.

The droplet evaporation process with electrowetting until the onset of nucleation (from t_n to t_e) was also analyzed for a varied frequency and amplitude. Representative data for each condition are shown in Figure 6. As shown in Figure 6a, when the amplitude is fixed at 60 V_{rms}, the final residue at 1 kHz consists of a single crystal, while residues at other frequencies form Type A or Type B agglomerates with tiny crystals. This observation can be attributed to the electrowetting-induced mixing effect. We hypothesize that in this study, the mixing effect is most prominent at 1 kHz. Previous research has demonstrated a strong frequency dependence of the internal flow. For aqueous droplets in ambient oil, an optimal mixing frequency of 50−100 Hz is observed, the frequency dependence of the flow explained by Stokes drift driven by capillary waves emanating from the oscillating contact line.[43] In contrast, for droplets in the air, the flow persists at higher frequencies. Frequencies in the low kHz range promote strong internal flows, with flow velocities reaching several hundred μm/s[31], which is attributed to the excitation of eigenmodes[44,45] and/or the propagation of capillary waves along the drop surface. Without internal mixing, the solute concentration near the contact line is expected to be higher than the average bulk concentration as the evaporation rate at the contact line is higher. With electrowetting at 1 kHz, we hypothesize that the time-dependent electrostatic force suppresses the pinning of the three-phase contact line and then enhanced mixing overcomes the evaporation-driven flow field within the droplets, thereby preventing the accumulation of solute along the contact line. This leads to a more homogeneous concentration within the droplet, which promotes crystal growth over nucleation, resulting in the Type C residue shape.

To evaluate the evaporation rate, we plotted the volume loss over time, as shown in Figure 6b. The droplet volume as a function of time is expressed as[46]

$$V(t)^{2/3} = V_0^{2/3} - kt \tag{4}$$

where k is a coefficient related to the diffusion coefficient of vapor in the air, the contact angle, relative humidity, liquid density, and the contact radius of the droplet.

At 100 kHz, the evaporation rate is higher than at other frequencies, as evidenced by the steeper slope, which is attributed to Joule heating.[47] Additionally, nucleation occurs earlier at 100 kHz due to the higher evaporation rate. For other frequencies, nucleation occurs earliest at 1 kHz, where S_{bulk} is the lowest. This explains the formation of the Type C residue at 1 kHz: with lower bulk supersaturation, fewer nuclei form within the droplet, promoting the growth of single crystals. In contrast, higher supersaturation (e.g., DC, 1 Hz, and 100 kHz) promotes the emergence of multiple small crystals that aggregate into agglomerates. No significant differences in the evaporation rate are observed for DC, 1 Hz, and 1 kHz. Since the experiment was conducted on the same day under ambient conditions, room temperature and humidity can be considered constant; therefore, the evaporation rate can be assumed to remain unchanged, which aligns with the findings.

With the frequency fixed at 1 kHz, the amplitude was varied from 20 to 80 V_{rms}, and the resulting residues are shown in Figure 6c. At 20 V_{rms}, Type B agglomerates formed, whereas at higher amplitudes, the residues are all Type C, consisting of either a single crystal or multiple single crystals on the millimeter scale. The droplet at 20 V_{rms} took longer to nucleate and reached a higher supersaturation compared to other cases

(Figure 6d). This is consistent with previous findings, where Type A or B nuclei form at a higher supersaturation. We offer two hypotheses to explain this observation. First, at lower amplitudes, internal mixing patterns are less prominent.[43] This suggests that a lower degree of mixing promotes a higher concentration difference between the bulk and the contact line, which, in turn, induces the formation of Type A and B residues. The second hypothesis relates to the electric field at the contact line. The induced-dipole interaction energy of an individual glycine molecule[4] is given by

$$U = \frac{1}{2}\Delta\alpha E^2 \simeq 1.1 \times 10^{-3}kT \tag{5}$$

where E is the electric field strength and $\Delta\alpha$ is the polarizability anisotropy of the glycine molecule. As shown in eq 5, the interaction energy is significantly smaller than the thermal energy (kT), indicating a weak direct alignment effect under the applied field. We assume that the electric field strength in the experiment is close to the dielectric strength of the Teflon layer ($\simeq 2 \times 10^8$ V/m).[30,35] When the electric field strength exceeds this value, Teflon will break down. This breakdown is evident in the experiment: at 60−80 V_{rms}, brown strip-like regions appear on the substrates at the end of the experiment, indicating that Teflon has broken down, as shown in Figure S4. In contrast, at 20−40 V_{rms}, many fewer brown strip-like regions are observed, suggesting that the electric field is insufficient to cause breakdown. Therefore, we suppose the electric field is close to the dielectric strength of Teflon layers, at least consistent in order of magnitude. Notably, the interaction energy is too weak to result in alignment of glycine molecules. However, the cooperative interactions among solute molecules in clusters have been suggested as a possible explanation for larger interaction energy.[4,48] At higher amplitudes, we speculate that a stronger electric field increases the induced-dipole interaction energy, thereby promoting the orderly arrangement of large solute clusters into a crystalline structure.

CONCLUSIONS

Polymorph control of glycine was achieved by evaporating sessile droplets under electrowetting (Figures 4 and 5). Without electrowetting, the final residue consists of hemispherical agglomerates with predominantly α-form glycine crystals (**Teflon-NO EW**). In contrast, electrowetting reduces the fraction of the α form while increasing the content of the γ form (**Teflon-EW**). As the electrowetting amplitude increases, the proportion of the Type C residue (single crystals) rises significantly. Notably, at 1 kHz and 80 V_{rms}, the final residue consists mainly of single crystals, predominantly in the γ form. We hypothesize that this is because electrowetting at 1 kHz promotes internal mixing and earlier nucleation. These two effects collectively create more homogeneous conditions and lower supersaturation compared to the **Teflon-NO EW** case. These conditions promote the growth of single crystals. The substrate surface also influences the polymorphic form. On the hydrophilic glass surface, the coffee stain residue consists of α and β forms (**Glass**), while on a hydrophobic Teflon surface, the hemispherical agglomerates are predominantly of the α form (**Teflon-NO EW**). This result demonstrates that electrowetting can effectively regulate the polymorphic form and morphology of glycine crystals, providing a promising method for high-throughput polymorph screening.

ASSOCIATED CONTENT

Supporting Information

The Supporting Information is available free of charge at https://pubs.acs.org/doi/10.1021/acs.cgd.5c00497.

Summary of the time-lapse crystallization images, images of all final residues, Raman spectra of glycine residues over time, droplet evaporation analysis, and videos of glycine droplets evaporating under three cases: **Glass**, **Teflon-NO EW**, and **Teflon-EW** (ZIP)

AUTHOR INFORMATION

Corresponding Author

Hüseyin Burak Eral − *Process & Energy Department, Delft University of Technology, Delft 2628 CB, The Netherlands;* orcid.org/0000-0003-3193-452X; Email: h.b.eral@tudelft.nl

Authors

Qi An − *Process & Energy Department, Delft University of Technology, Delft 2628 CB, The Netherlands;* orcid.org/0009-0003-9458-2880

Pingping Cui − *Process & Energy Department, Delft University of Technology, Delft 2628 CB, The Netherlands; School of Chemical Engineering and Technology, Tianjin University, Tianjin 300072, China*

Nagaraj Nagalingam − *Process & Energy Department, Delft University of Technology, Delft 2628 CB, The Netherlands;* orcid.org/0000-0003-4497-3691

Noah Binan − *Department of Chemical Engineering, Delft University of Technology, Delft 2629 HZ, The Netherlands*

Bijoy Bera − *Department of Chemical Engineering, Delft University of Technology, Delft 2629 HZ, The Netherlands;* orcid.org/0000-0002-8626-3682

Massimo Mastrangeli − *Department of Microelectronics, Delft University of Technology, Delft 2628 CD, The Netherlands*

Johan T. Padding − *Process & Energy Department, Delft University of Technology, Delft 2628 CB, The Netherlands;* orcid.org/0000-0003-4161-0748

Complete contact information is available at: https://pubs.acs.org/10.1021/acs.cgd.5c00497

Notes

The authors declare no competing financial interest.

ACKNOWLEDGMENTS

The authors thank Ali Murat Sağlam for his assistance in the experiment and Assoc. Prof. Sevgi Polat for insightful discussions. Q. An thanks the China Scholarship Council for the scholarship.

REFERENCES

(1) Ibis, F.; Nuhu, M. A.; Penha, F. M.; Yu, T. W.; van Der Heijden, A. E.; Kramer, H. J.; Eral, H. B. Role of hyaluronic acid on the nucleation kinetics of calcium oxalate hydrates in artificial urine quantified with droplet microfluidics. *Cryst. Growth Des.* **2022**, *22*, 3834−3844.

(2) Lewis, A.; Seckler, M.; Kramer, H.; Van Rosmalen, G. *Industrial Crystallization: Fundamentals and Applications*; Cambridge University Press, 2015.

(3) Yuan, Z.; Wang, L.; Wu, M.; Niu, Y.; Meng, Y.; Ruan, X.; He, G.; Jiang, X. Confined liquid crystallization governed by electric field for API crystal polymorphism screening and massive preparation. *J. Colloid Interface Sci.* **2024**, *664*, 74−83.

(4) Aber, J. E.; Arnold, S.; Garetz, B. A.; Myerson, A. S. Strong dc electric field applied to supersaturated aqueous glycine solution induces nucleation of the γ polymorph. *Physical review letters* **2005**, *94*, 145503.

(5) Li, F.; Lakerveld, R. Electric-field-assisted protein crystallization in continuous flow. *Cryst. Growth Des.* **2018**, *18*, 2964−2971.

(6) Polat, S.; Sayan, P. Effect of ultrasonic irradiation on morphology and polymorphic transformation of glycine. *Ultrason. Sonochem.* **2018**, *47*, 17−28.

(7) Gracin, S.; Uusi-Penttilä, M.; Rasmuson, Å. C. Influence of ultrasound on the nucleation of polymorphs of p-aminobenzoic acid. *Cryst. Growth Des.* **2005**, *5*, 1787−1794.

(8) Belca, L. M.; Ručigaj, A.; Teslič, D.; Krajnc, M. The use of ultrasound in the crystallization process of an active pharmaceutical ingredient. *Ultrason. Sonochem.* **2019**, *58*, 104642.

(9) Bai, C.; Wang, C.; Zheng, T.; Hu, Q. Growth of β-glycine crystals promoted by standing surface acoustic waves (SSAWs). *CrystEngComm* **2018**, *20*, 1245−1251.

(10) Penha, F. M.; Gopalan, A.; Meijlink, J. C.; Ibis, F.; Eral, H. B. Selective crystallization of d-mannitol polymorphs using surfactant self-assembly. *Cryst. Growth Des.* **2021**, *21*, 3928−3935.

(11) Carter, P. W.; Ward, M. D. Topographically directed nucleation of organic crystals on molecular single-crystal substrates. *J. Am. Chem. Soc.* **1993**, *115*, 11521−11535.

(12) Nagalingam, N.; Raghunathan, A.; Korede, V.; Poelma, C.; Smith, C. S.; Hartkamp, R.; Padding, J. T.; Eral, H. B. Laser-Induced Cavitation for Controlling Crystallization from Solution. *Physical review letters* **2023**, *131*, 124001.

(13) Irimia, D.; Jose Shirley, J.; Garg, A. S.; Nijland, D. P.; van der Heijden, A. E.; Kramer, H. J.; Eral, H. B. Influence of laser parameters and experimental conditions on nonphotochemical laser-induced nucleation of glycine polymorphs. *Cryst. Growth Des.* **2021**, *21*, 631−641.

(14) Korede, V.; Nagalingam, N.; Penha, F. M.; van der Linden, N.; Padding, J. T.; Hartkamp, R.; Eral, H. B. A review of laser-induced crystallization from solution. *Cryst. Growth Des.* **2023**, *23*, 3873−3916.

(15) Hernandez Espinell, J. R.; López-Mejías, V.; Stelzer, T. Revealing polymorphic phase transformations in polymer-based hot melt extrusion processes. *Cryst. Growth Des.* **2018**, *18*, 1995−2002.

(16) Selekman, J. A.; Qiu, J.; Tran, K.; Stevens, J.; Rosso, V.; Simmons, E.; Xiao, Y.; Janey, J. High-throughput automation in chemical process development. *Annu. Rev. Chem. Biomol. Eng.* **2017**, *8*, 525−547.

(17) Pfund, L. Y.; Matzger, A. J. Towards exhaustive and automated high-throughput screening for crystalline polymorphs. *ACS combinatorial science* **2014**, *16*, 309−313.

(18) Gui, Y. Solid form screenings in pharmaceutical development: A perspective on current practices. *Pharm. Res.* **2023**, *40*, 2347−2354.

(19) Perlovich, G.; Hansen, L. K.; Bauer-Brandl, A. The polymorphism of glycine. Thermochemical and structural aspects. *J. Therm. Anal. Calorim.* **2001**, *66*, 699−715.

(20) Lee, A. Y.; Lee, I. S.; Dette, S. S.; Boerner, J.; Myerson, A. S. Crystallization on confined engineered surfaces: A method to control crystal size and generate different polymorphs. *J. Am. Chem. Soc.* **2005**, *127*, 14982−14983.

(21) Guerin, S.; Stapleton, A.; Chovan, D.; Mouras, R.; Gleeson, M.; McKeown, C.; Noor, M. R.; Silien, C.; Rhen, F. M.; Kholkin, A. L.; et al. Control of piezoelectricity in amino acids by supramolecular packing. *Nature materials* **2018**, *17*, 180−186.

(22) Seyedhosseini, E.; Ivanov, M.; Bystrov, V.; Bdikin, I.; Zelenovskiy, P.; Shur, V. Y.; Kudryavtsev, A.; Mishina, E. D.; Sigov, A. S.; Kholkin, A. L. Growth and nonlinear optical properties of β-glycine crystals grown on Pt substrates. *Cryst. Growth Des.* **2014**, *14*, 2831−2837.

(23) Poornachary, S. K.; Parambil, J. V.; Chow, P. S.; Tan, R. B.; Heng, J. Y. Nucleation of elusive crystal polymorphs at the solution−substrate contact line. *Cryst. Growth Des.* **2013**, *13*, 1180−1186.

(24) Boyes, M.; Alieva, A.; Tong, J.; Nagyte, V.; Melle-Franco, M.; Vetter, T.; Casiraghi, C. Exploiting the surface properties of graphene for polymorph selectivity. *ACS Nano* **2020**, *14*, 10394−10401.

(25) He, G.; Bhamidi, V.; Tan, R. B.; Kenis, P. J.; Zukoski, C. F. Determination of critical supersaturation from microdroplet evaporation experiments. *Cryst. Growth Des.* **2006**, *6*, 1175−1180.

(26) Kim, K.; Centrone, A.; Hatton, T. A.; Myerson, A. S. Polymorphism control of nanosized glycine crystals on engineered surfaces. *CrystEngComm* **2011**, *13*, 1127−1131.

(27) Lee, I. S.; Kim, K. T.; Lee, A. Y.; Myerson, A. S. Concomitant crystallization of glycine on patterned substrates: The effect of pH on the polymorphic outcome. *Cryst. Growth Des.* **2008**, *8*, 108−113.

(28) Buanz, A. B.; Gaisford, S. Formation of highly metastable β glycine by confinement in inkjet printed droplets. *Cryst. Growth Des.* **2017**, *17*, 1245−1250.

(29) Slabov, V.; Vasileva, D.; Keller, K.; Vasilev, S.; Zelenovskiy, P.; Kopyl, S.; Shur, V. Y.; Vinogradov, A.; Kholkin, A. Controlled growth of stable β-glycine via inkjet printing. *Cryst. Growth Des.* **2019**, *19*, 3869−3875.

(30) Mugele, F.; Baret, J.-C. Electrowetting: from basics to applications. *J. Phys.: Condens. Matter* **2005**, *17*, R705.

(31) Eral, H. B.; Augustine, D. M.; Duits, M. H.; Mugele, F. Suppressing the coffee stain effect: how to control colloidal self-assembly in evaporating drops using electrowetting. *Soft Matter* **2011**, *7*, 4954−4958.

(32) Mampallil, D.; Eral, H. B. A review on suppression and utilization of the coffee-ring effect. *Advances in colloid and interface science* **2018**, *252*, 38−54.

(33) Kudina, O.; Eral, B.; Mugele, F. e-MALDI: an electrowetting-enhanced drop drying method for MALDI mass spectrometry. *Analytical chemistry* **2016**, *88*, 4669−4675.

(34) Kudina, O.; Eral, H. B.; Mugele, F. E-MALDI: optimized conditions during electrowetting-enhanced drop drying for MALDI-MS. *J. Mass Spectrom.* **2017**, *52*, 405−410.

(35) Seyrat, E.; Hayes, R. A. Amorphous fluoropolymers as insulators for reversible low-voltage electrowetting. *J. Appl. Phys.* **2001**, *90*, 1383−1386.

(36) Deegan, R. D.; Bakajin, O.; Dupont, T. F.; Huber, G.; Nagel, S. R.; Witten, T. A. Capillary flow as the cause of ring stains from dried liquid drops. *Nature* **1997**, *389*, 827−829.

(37) Mullin, J. W. *Crystallization*; Elsevier, 2001.

(38) Eral, H. B.; 't Mannetje, D.; Oh, J. M. Contact angle hysteresis: a review of fundamentals and applications. *Colloid and polymer science* **2013**, *291*, 247−260.

(39) Marin, A. G.; Gelderblom, H.; Lohse, D.; Snoeijer, J. H. Order-to-disorder transition in ring-shaped colloidal stains. *Physical review letters* **2011**, *107*, 085502.

(40) Wu, Y.; Xiong, N.; Liu, Y.; Xie, T.; Zhao, Q.; Li, G. Static and Surfactant-Free Quasi-Double Emulsions as Programmable Micro-crystallizers for Controllable Polymorphic Crystallization. *Cryst. Growth Des.* **2022**, *22*, 5416−5423.

(41) Lee, S.; Wi, H. S.; Jo, W.; Cho, Y. C.; Lee, H. H.; Jeong, S.-Y.; Kim, Y.-I.; Lee, G. W. Multiple pathways of crystal nucleation in an extremely supersaturated aqueous potassium dihydrogen phosphate (KDP) solution droplet. *Proc. Natl. Acad. Sci. U.S.A.* **2016**, *113*, 13618−13623.

(42) Bonn, D.; Shahidzadeh, N. Multistep crystallization processes: How not to make perfect single crystals. *Proc. Natl. Acad. Sci. U.S.A.* **2016**, *113*, 13551−13553.

(43) Mugele, F.; Staicu, A.; Bakker, R.; van den Ende, D. Capillary Stokes drift: a new driving mechanism for mixing in AC-electrowetting. *Lab Chip* **2011**, *11*, 2011.

(44) Ko, S. H.; Lee, S. J.; Kang, K. H. A synthetic jet produced by electrowetting-driven bubble oscillations in aqueous solution. *Appl. Phys. Lett.* **2009**, *94*, 194102.

(45) Mampallil, D.; van den Ende, D.; Mugele, F. Controlling flow patterns in oscillating sessile drops by breaking azimuthal symmetry. *Applied physics letters* **2011**, *99*, 154102.

(46) Seyfert, C.; Berenschot, E. J.; Tas, N. R.; Susarrey-Arce, A.; Marin, A. Evaporation-driven colloidal cluster assembly using droplets on superhydrophobic fractal-like structures. *Soft Matter* **2021**, *17*, 506−515.

(47) García-Sánchez, P.; Ramos, A.; Mugele, F. Electrothermally driven flows in ac electrowetting. *Physical Review E—Statistical, Nonlinear, and Soft Matter Physics* **2010**, *81*, 015303.

(48) Oxtoby, D. W. Crystals in a flash. *Nature* **2002**, *420*, 277−278.